A Tri-Mode Photothermal, Phase-Change, and Radiative-Cooling Film for All-Day Thermoelectric Generation

Mingtai Hou, Hao Chen, Song Li, Xinru Zhang, Jie Chen, Zeyi Jiang,* Cunhai Wang,* Nien-Chu Lai,* and Yulong Ding

Solar-thermal-electric conversion shows great promise, especially in off-grid aerospace and navigation. However, low output density and intermittency of solar energy limit its application. Herein, a microencapsulated phase change material (MPCMs) is designed with a n-Tetracosane core and TiO_2/Ti_2O_3 composite shell to address the above issue. The MPCM exhibits a latent heat of 144.5 $J g^{-1}$, a photothermal conversion efficiency of 93.7% and 100% energy storage capacity. The thermoelectric system resulting from coupling the multifunctional film composed of polydimethylsiloxane and MPCMs with the thermoelectric module is capable of successfully achieving adaptive 24 h uninterrupted power generation on account of its functions of photothermal conversion, energy storage, and radiative cooling. The output power density of the TES ranged from 6.1 to 21.1 $W m^{-2}$ at light intensities of 1000–5000 $W m^{-2}$. The material design innovatively endows a single material with the functions of photothermal conversion, phase change energy storage, and radiative cooling, making it can adaptively harvest energy from both the sun and cold space. This multifunctional material offers new insights into the repeatable storage and high-quality utilization of solar energy, holding significant scientific implications for the development of all-day solar-thermal-electric power generation technology.

1. Introduction

In view of the environmental pollution and ecological disruption resulting from the current excessive dependence on fossil energy, the development and efficient utilization of renewable and clean energy have emerged as the most pressing scientific and engineering challenges. Converting renewable energy into electricity has been a long-sought research goal for scientists over the past century.[1] Thermoelectric generators (TEGs) directly transform thermal energy into electrical energy by exploiting thermally excited carriers, and they are characterized by fuel-free operation, no vibration, low cost, and long service life.[2] The TEG technology has received widespread attention in high-tech domains like aerospace.[3] Efficiently converting the sunlight that bathes the Earth into thermal energy is the most cost-effective and environmentally friendly way to utilize solar energy. In recent years, the rapid advancement of photothermal conversion (PTC), passive radiative cooling (RC) technologies, and the adaptive switching between daytime PTC and night-time RC has been realized, offering a significant reference for enhancing the efficiency and prolonging the service life of TEGs.[4] Nevertheless, due to the intermittent and low energy density characteristics of solar radiation, achieving genuine 24 h continuous power generation remains a challenge.

Microencapsulated phase change materials (MPCMs) composed of organic PCMs as the core and high thermal conductivity and full-spectrum absorption materials as the shell are the

M. Hou, H. Chen, X. Zhang, Z. Jiang, C. Wang, N.-C. Lai
School of Energy and Environmental Engineering
University of Science and Technology Beijing
Beijing 100083, China
E-mail: zyjiang@ustb.edu.cn; wangcunhai@ustb.edu.cn;
nclai@ustb.edu.cn
S. Li
Key Laboratory of Thermo-Fluid Science and Engineering
Ministry of Education
Xi'an Jiaotong University
Xi'an 710049, China

Z. Jiang
Beijing Key Laboratory for Energy Saving and Emission Reduction of
Metallurgical Industry
Beijing 100083, China
N.-C. Lai
Beijing Engineering Research Center of Energy Saving and Environmental
Protection
Beijing 100083, China
J. Chen, Y. Ding
Birmingham Centre for Energy Storage
School of Chemical Engineering
University of Birmingham
Birmingham B15 2TT, UK
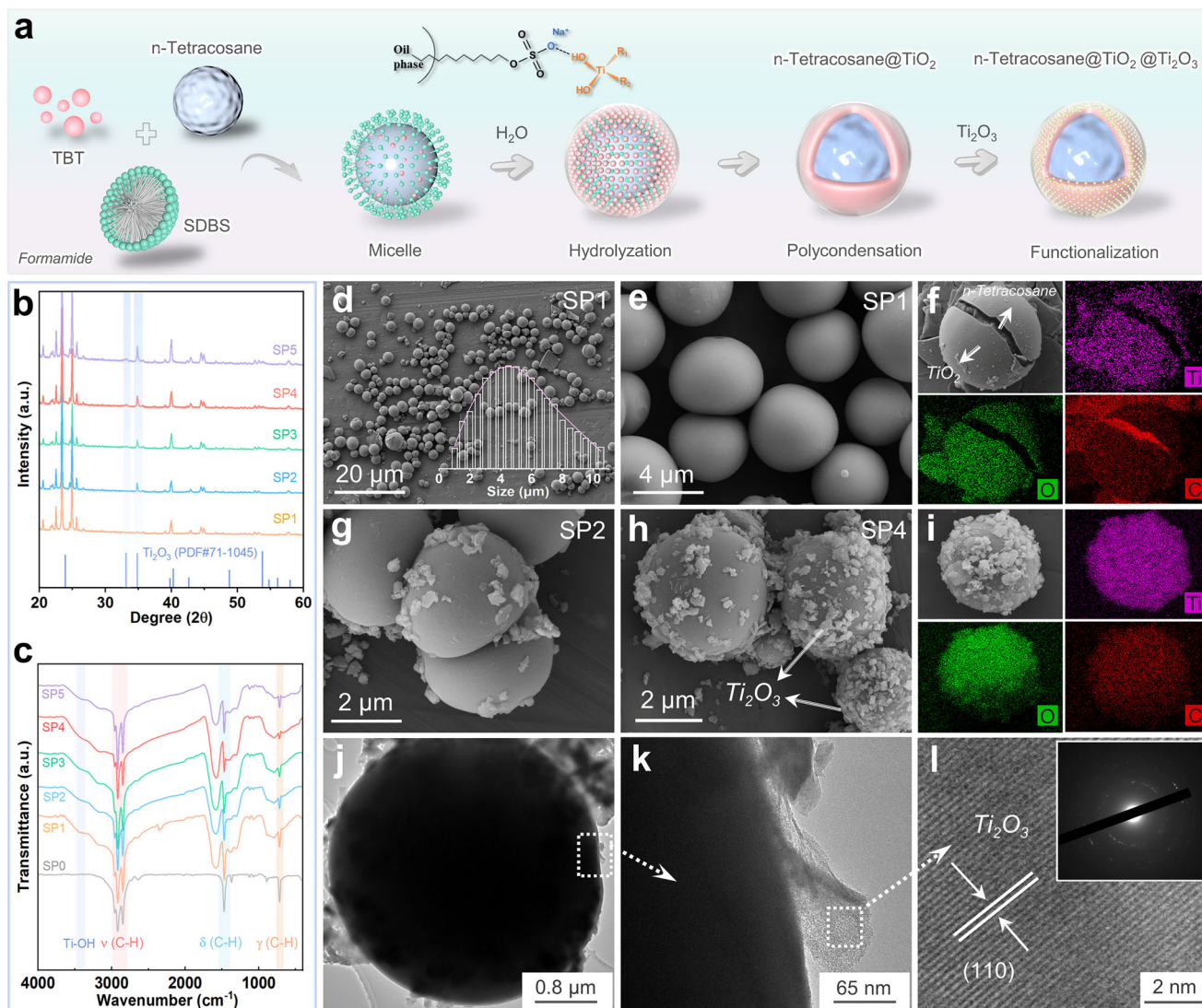
Figure 1. Preparation and characterization of microcapsules. a) Schematic diagram for preparing the n-Tetracosane@TiO$_2$/Ti$_2$O$_3$ composite microcapsules. b) XRD patterns of SP1-SP5. c) FTIR spectra of SP0-SP5. d,e) Morphologies of SP1 (The inset shows the particle size distribution of microcapsules). f) Morphologies and EDX images of the crushed microcapsules. g) Morphologies of SP2. h) Morphologies and i) EDX images of SP4. j–l) TEM micrographs of SP4.

ideal composite materials for achieving high energy density and long-term reliability in PTC technology.[5] As a common shell material featuring high encapsulation efficiency,[6] TiO$_2$ has been widely acknowledged as a material with great potential in nighttime RC applications in recent years, owing to its remarkable thermal radiation performance in the atmospheric transparent window region.[7] Unlike its stoichiometric oxide counterpart, oxygen-vacancy non-stoichiometric TiO$_{2-x}$ possesses a high density of free carriers and exhibits metal-like localized surface plasmon resonance (LSPR) properties, thereby demonstrating strong full-spectrum absorption performance and rendering it an efficient PTC material.[8] To date, no literature has reported on the combination of defective TiO$_{2-x}$ with a titanium-based shell as a shell material for efficient photothermal MPCMs. This is primarily due to the mismatch between the high-temperature conditions

required for TiO$_{2-x}$ preparation and the synthesis conditions of MPCMs.

Herein, we report a meticulously designed full-spectrum photothermal MPCM composed of n-Tetracosane encapsulated in a TiO$_2$/Ti$_2$O$_3$ composite shell (designated as n-Tetracosane@TiO$_2$/Ti$_2$O$_3$). The innovation lies in the clever combination of TiO$_2$ and Ti$_2$O$_3$ through Ti—O—Ti bonds. This composite shell design endows microcapsules with high encapsulation efficiency, high photothermal conversion efficiency (PTCE), and high emissivity. n-Tetracosane@TiO$_2$/Ti$_2$O$_3$ microcapsules exhibited a latent heat of 144.5 J g^{-1} and a complete (100%) energy storage capacity. Owing to the strong LSPR effect of Ti$_2$O$_3$, the PTCE of n-Tetracosane@TiO$_2$/Ti$_2$O$_3$ can reach as high as 93.7%. Benefiting from the abundant Ti—OH groups on the surface of the oxide shell, we fabricate a composite film material by

compounding the MPCMs with polydimethylsiloxane (PDMS). The prepared composite thin-film material can operate in three modes: photothermal, phase change storage and release, and radiative cooling. It has an absorptivity of 93.91% within the solar spectrum, and emissivities of 93.81% and 93.82% in the first and second atmospheric windows, respectively.

The composite film is further integrated into a BiTe TEG for 24 h uninterrupted electricity generation. When exposed to an illumination of 5000 W m^{-2}, the composite film-integrated thermoelectric system (TES) can attain a maximum output voltage (V_o) of 749.1 mV. When the external illumination is removed, the TES can still sustain discharge for more than 800 s by releasing the stored thermal energy in the MPCM. At night, the TES with the RC functionality is capable of continuously generating electricity under subambient temperature conditions. The outdoor experimental outcomes in different cities indicate that our TES exhibits universal and stable power generation capabilities. During the daytime, the maximum temperature difference and power generation amount respectively reach 23.2 °C and 164.3 mV; whereas at night, these two values are 3.5 °C and 18.9 mV, respectively, enabling all-day thermoelectric generation through the synergistic integration of PTC, phase-change, and RC effects. This research offers a new perspective for the development and application of high-performance multi-functional MPCMs.

2. Results and Discussion

2.1. Chemical Composition and Crystalline Structure of Microcapsules

To achieve the desired morphology of core–shell MPCMs, we prepared SP1 (n-Tetracosane@TiO$_2$) employing an interfacial polymerization method.[5a,c,9] The schematic diagram and reaction mechanism of the synthesis process were illustrated in **Figure 1a**. The presence of regular monodisperse droplets was verified via an optical microscope, which indicated the successful emulsification of the oil phase containing n-Tetracosane and tetrabutyl titanate (TBT) in formamide (Figure S1, Supporting Information). A small quantity of water was introduced into the reaction solution to initiate the hydrolysis and polycondensation of TBT on the surface of the emulsion droplets, ultimately forming a dense amorphous shell of TiO$_2$ at the interface. Eventually, the samples were collected via filtration and drying. The SP2-SP5 microcapsules were fabricated by adding varying contents of Ti$_2$O$_3$ nanoparticles (NPs) to the synthesized SP1 sample. The chemical structure of the MPCMs was characterized using X-ray diffraction (XRD) and Fourier Transform Infrared (FTIR) spectrometer analysis (Figure 1b,c). In the MPCMs, apart from the characteristic peaks of the n-Tetracosane at 2θ angles less than 30 degrees,[10] the diffraction peaks of Ti$_2$O$_3$ crystals (PDF No. 71–1045) were also detected. FTIR spectra revealed that the alkyl C—H stretching vibrations corresponding to methyl and methylene groups appeared at 2960, 2916, and 2845 cm^{-1}, respectively, and the bending vibrations occurred at 1472 and 719 cm^{-1}, which are in accordance with the characteristic bands of the organic PCM.[10–11] The microstructure and elemental distribution of the MPCMs were characterized employing scanning electron microscopy (SEM), energy dispersive X-ray spectroscopy (EDX), and transmission

electron microscopy (TEM) (Figure 1j–l). Figure 1d shows the particle size distribution of the MPCMs, among which the majority range from 4 to 5 micrometers. Through elemental mapping analysis (Figure 1f,i; Figure S2, Supporting Information), it was verified that the MPCMs possessed a core–shell structure composed of an organic core and titanium oxide shell. The TEM results indicated that the irregular nanoparticles on the surface of the MPCM were Ti$_2$O$_3$ (Figure S3, Supporting Information), and Figure 1k,l indicating that the main exposed crystal plane was the (110) facet. It is reasonable to infer that the abundant Ti—OH groups on the surface of TiO$_2$ might be the main driving force for the adhesion of Ti$_2$O$_3$ NPs onto the surface of the MPCMs. The XPS survey-spectrum analysis of MPCM was carried out and shown in Figure S4 (Supporting Information). The high-resolution Ti 2p spectrum of SP1 exhibited pronounced signals at 458.4 and 464.3 eV, corresponding to 2p$_{3/2}$ and 2p$_{1/2}$ of Ti (IV), respectively.[12] However, the high-resolution Ti 2p spectrum of SP4 could be deconvoluted into four peaks. Apart from the two peaks associated with Ti (IV), the remaining two peaks were located at 457.6 and 463.9 eV, corresponding to Ti (III).[13] The high-resolution O 1s XPS spectrum of SP4 displayed three peaks at 529.6, 530.9, and 531.7 eV, which were respectively associated with Ti—O (TiO$_2$), Ti—O (Ti$_2$O$_3$) and —OH.[12] The aforementioned characterization results verified that n-Tetracosane has been successfully encapsulated within the TiO$_2$ shell, and the shell surface was embedded with unevenly distributed Ti$_2$O$_3$ NPs.

2.2. Thermal Energy Storage and Photothermal Stability Properties of Microcapsules

To investigate the thermal behavior of the pure n-Tetracosane (SP0) and MPCMs (SP1-SP5), we employed differential scanning calorimetry (DSC) for analysis, and the results are shown in **Figures 2a** and S5, and Table S1 (Supporting Information). Compared with the SP1 sample with a latent heat of 187.9 J g^{-1}, the latent heat of the SP2–SP5 samples gradually decreased to 136.7–169.9 J g^{-1} with the increase of the loading amount of Ti$_2$O$_3$ NPs. Utilizing Equations (1–3), we calculated the key parameters of the MPCMs, including encapsulation efficiency (E_{en}), latent heat storage efficiency (E_{es}), and energy storage capacity (C_{es}). Among them, C_{es} is used to quantify the ratio of PCM in microcapsules that can undergo reversible phase change and is a crucial indicator for evaluating the heat storage efficiency of microcapsules.[6,14] Based on to the data in Table S1 (Supporting Information), the C_{es} for SP1–SP5 is ≈100%. This implies that the C_{es} value is more closely related to the tight encapsulation of the TiO$_2$ shell rather than being affected by the addition of Ti$_2$O$_3$ particles. Experimental results show that the modification of photothermal materials on the surface of the shell material has a negligible effect on the reversibility of the PCM core. The DTG curve indicated that the maximum thermal degradation temperature (T_{max}) of the MPCMs was ≈290 °C, significantly higher than that of SP0 (Figure 2b). Evidently, the core–shell structure effectively protects the PCM core from thermal decomposition. This not only verifies that the prepared MPCMs possess outstanding thermal stability but also indicates that they have considerable heat storage capacity.
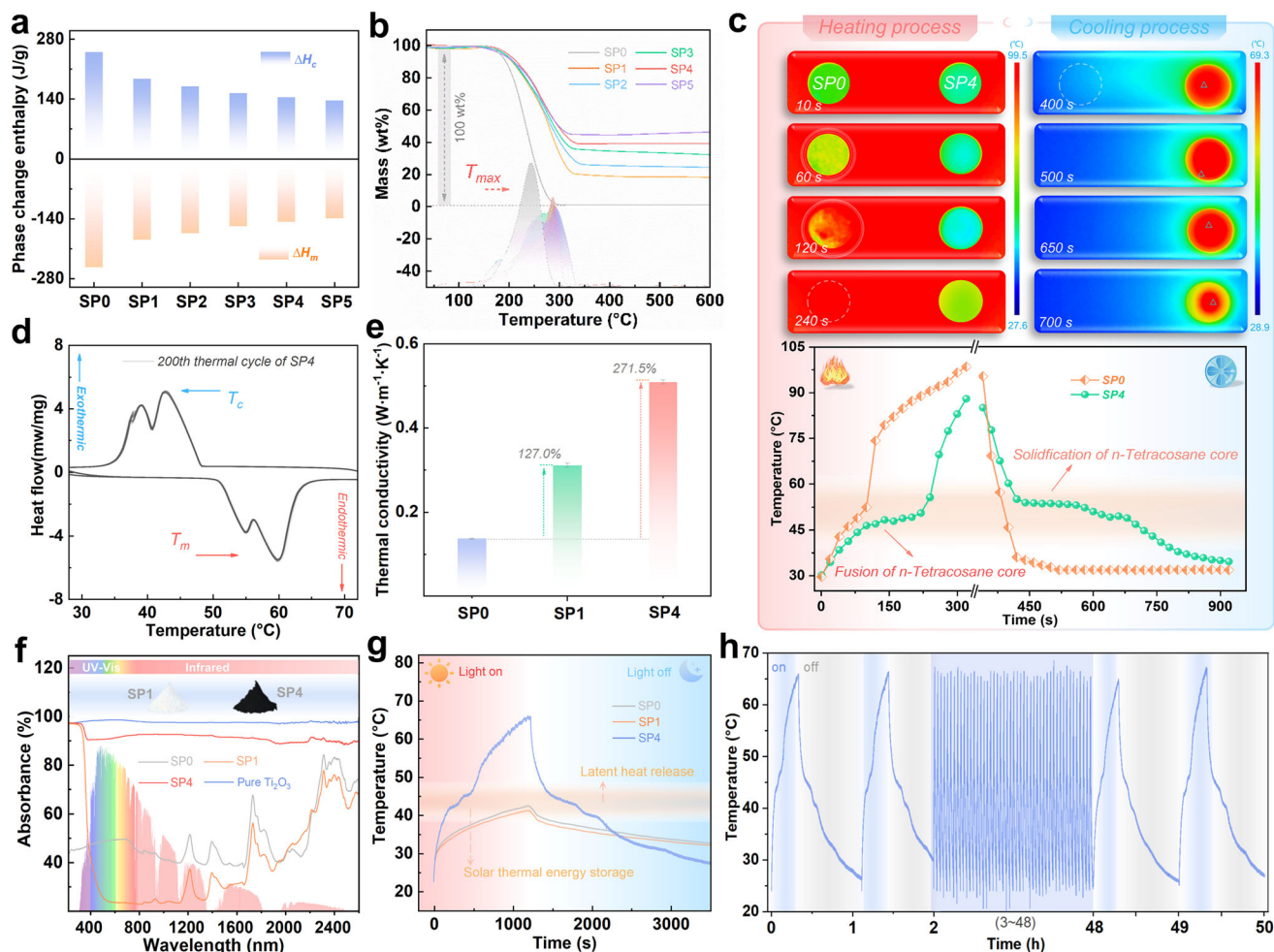
Figure 2. Thermal energy storage and photothermal stability properties. a) Phase change enthalpies of n-Tetracosane (SP0) and MPCMs (SP1-SP5). b) TGA and DTG thermograms of SP0–SP5. c) IR images and temperature distribution curves of SP0 and SP4 during heating and cooling processes. The plateaus in the temperature curves indicate the phase change stages of n-Tetracosane. d) Multicycle DSC diagrams of SP4. e) Thermal conductivity of SP0, SP1, and SP4. f) Optical images and UV–vis–NIR absorption spectra of Ti_2O_3, SP0, SP1, and SP4. g) The temperature-time curves of SP0, SP1, and SP4. h) Temperature curves of SP4 during fifty lighting-cooling cycles.

To explore the thermal regulation and leakage behavior of the MPCMs, 0.3 g of SP0 and SP4 were compressed into discs with a diameter of 1.5 cm and a thickness of 3 mm and subjected to testing on a ceramic heating plate (Figure S6a, Supporting Information). The outcomes revealed that the SP0 disc completely melted after 240 s of heating due to phase change, whereas the SP4 disc maintained its shape throughout the heating process, indicating no obvious leakage during heating. Furthermore, the remarkable phase change heat storage performance of SP4 could be visually observed through color alterations. The temperature-time curve at the bottom of Figure 2c indicates a distinct temperature plateau ≈50 °C during the heating and cooling of SP4, which was associated with the phase change characteristics of the n-Tetracosane core. To assess the thermal reliability of SP4, multiple DSC cycling experiments were carried out. The results demonstrated that after 200 thermal cycles, the DSC curve of SP4 displayed outstanding phase change reversibility and thermal stability (Figure 2d), with the heat flow peaks, phase change enthalpy, and temperature of each scan being nearly identical

(Figures S6b, S7a, Supporting Information). To further validate its structural stability, FTIR and SEM were employed to analyze the changes of SP4 before and after the thermal cycling experiment (Figure S7b,c, Supporting Information). The results showed that the functional groups and morphology of SP4 were highly coincident before and after the thermal cycling, indicating that its chemical structure and morphology remained essentially unchanged. In Figure 2e, the thermal conductivity of SP1 amounted to 0.311 W m^{-1} K^{-1}, which was 127.0% higher than that of SP0 at 0.137 W m^{-1} K^{-1}. When the loading amount of Ti_2O_3 is 5%, the thermal conductivity of the SP4 sample attained 0.509 W m^{-1} K^{-1}, representing an increase of 271.5% compared to SP0.

The UV–vis–NIR spectroscopy was employed to determine the absorbance of the MPCMs and assess their PTC performance (Figure 2f–h; Figure S8, Supporting Information). We recorded its reflectance (ρ), transmittance (τ), and calculated its emissivity (ε) for each sample using Equation (4). According to Kirchhoff's radiation law, the spectral emissivity is equal to the spectral

**ADVANCED
SCIENCE NEWS**

www.advancedsciencenews.com

**ADVANCED
MATERIALS**

www.advmat.de

absorptivity in thermodynamic equilibrium.[15] Owing to the outstanding light absorption characteristics of Ti_2O_3 NPs, the composite MPCMs exhibited strong absorption capability across the entire spectral range. The PTC and heat storage performance of MPCMs were evaluated through a self-built PTC system (Figure S8b, Supporting Information). Under illumination conditions, all the SP2–SP5 microcapsules exhibited excellent photothermal properties (Figure 2g; Figure S8c, Supporting Information). In contrast to the SP0 and SP1 control samples, the SP2-SP5 microcapsules showed a more rapid temperature rise under light illumination. During the processes of both light irradiation and cooling, all samples demonstrated latent heat plateaus contributed by the phase transition of n-Tetracosane. Based on the characteristics of the phase transition plateaus, the PTCE (η) of the microcapsules could be calculated via Equation (5). The η values of the SP2 to SP5 samples were respectively from 74.2% to 95.6% (Table S2, Supporting Information). Compared to the photothermal MPCMs reported in the literature, SP4 exhibits highly competitive PTCE (Table S3, Supporting Information). The outcomes of 50 iterative cycles indicated that SP4 showed outstanding photothermal reversibility and reliability (Figure 2h). The time-temperature curve remained nearly invariant, and the peak temperature fluctuation was controlled within ±1.2 °C. The infrared thermography in Figure S9 (Supporting Information) presented the comparison of photothermal performance between SP1 and SP4 under the identical illumination conditions. After 20 min, the surface temperature of SP4 ascended to 65.5 °C, which was significantly higher than that of SP1 (41.6 °C). These results further validated the superior PTC capacity of Ti_2O_3.

2.3. Preparation and Characterization of Composite Films

To make the n-Tetracosane@TiO_2/Ti_2O_3 microcapsules applicable to a wider range of scenarios, we uniformly blended SP4 microcapsules with the PDMS precursor via hydrogen bonds by exploiting the abundant Ti—OH groups on their surface, thereby preparing a tri-mode film (i.e., TMF@SP4) capable of operating in three modes: photothermal conversion, phase change energy storage, and radiative cooling. PDMS is a transparent polymer that is extensively used in the domain of film materials due to its high resistance to UV degradation and chemical inertness toward water and oxidants.[16] The detailed preparation procedure of TMF@SP4 is illustrated in Figure S10 (Supporting Information). As illustrated in **Figure 3a**, TMF@SP4-2, which contains 60 wt.% SP4 microcapsules exhibited a black and opaque appearance compared to pure PDMS films. X-ray diffraction topography analysis revealed a dense arrangement of microcapsules in the bottom layer of the film, likely attributed to density differences during the film formation process (Figure 3b). This dense packing of photothermal microcapsules facilitates the establishment of effective thermal conduction pathways within the film material. Moreover, the film achieved dual encapsulation of PCMs, effectively mitigating leakage and corrosion, thereby expanding the application of PCMs in wearable devices and thermal management. Owing to its excellent flexibility, TMF@SP4-2 can be bent and rolled into various shapes (Figure 3c). SEM and EDX images demonstrated the microcapsules and elemental distribution on the top surface and cross-section of the composite film. The SEM images indicated that the top surface of the film was primarily composed of PDMS, exhibiting a porous structure. EDX results reveal the dispersion of microcapsules within the porous structure (Figure 3d; Figure S11, Supporting Information). Figure 3e shows that the FTIR spectrum of TMF@SP4-2 exhibits peaks at 2924 and 2852 cm^{-1}, corresponding to the stretching vibrations of —CH_2 and —CH_3 in SP0, respectively, while the peak at 1084 cm^{-1} is attributed to the asymmetric stretching vibration of Si—O—Si. The peak at 1084 cm^{-1} is ascribed to the asymmetric stretching vibration of Si—O—Si. Notably, the hydroxyl peak of SP4 originally observable in the range of 3745–3060 cm^{-1} has vanished in the FTIR spectrum of the composite film. This phenomenon could be attributed to the formation of hydrogen bonds between the Ti—OH groups on the surface of SP4 and the Si—OH groups in the PDMS precursor. The formation of such hydrogen bonds not only effectively reduces the interfacial thermal resistance but also facilitates heat transfer within the composite film.[17] The thermal conductivity tests in Figure S12 (Supporting Information) showed that the thermal transfer performance of TMF@SP4-2 is significantly enhanced after the introduction of SP4, with a thermal conductivity of 0.344 W m^{-1} K^{-1}, which is 67.1% higher than that of pure PDMS film (0.206 W m^{-1} K^{-1}). To further clarify the interaction between PDMS and MPCM, XPS was used to characterize the elemental composition and electronic state of TMF@SP4-2 (Figure S13, Supporting Information). In contrast to the prominent hydroxyl signal in the SP4 powders (*cf.* Figure S4c, Supporting Information), the existence of hydroxyl groups was not detectable in the high-resolution O 1s spectrum of TMF@SP4-2. Instead, a distinct peak was observed at 532.3 eV, which was attributed to the formation of Si—O—Ti bonds.[18] The thermal storage capacity of TMF@SP4 was also analyzed by DSC (Figure 3f; Figure S14, Supporting Information). The results indicated that the crystallization temperatures of the composite films with different MPCM mass fractions (40–80%) ranged from 30 to 50 °C, the melting temperatures were between 50 and 65 °C, and the enthalpy values were in the range of 104.3–45.6 J g^{-1}. Through heating-cooling tests, the temperature-time curves clearly showed a temperature plateau ≈50 °C for the TMF@SP4-2 film, corresponding to the phase transition process of n-Tetracosane (Figure S15, Supporting Information). To further quantify the leakage of the PCM, the TMF@SP4-2 film was placed on a hot plate above the phase change temperature with a 500 g weight applied and underwent 10 heating-cooling cycles. Benefiting from the dual encapsulation, the mass loss of the TMF@SP4-2 film was less than 0.1% after 10 cycles (Figure S16, Supporting Information). Furthermore, TMF@SP4-2 also exhibited intense absorption over the entire spectral range and demonstrated outstanding PTC performance (Figures S17, S18, Supporting Information). TMF@SP4-2 was subjected to fifty repetitive photo-thermal cycles (Figure 3g), and its photothermal performance was tested after bending fifty times to confirm the mechanical stability (Figure 3h). Figure 3i shows the infrared thermal imaging of the "USTB" pattern tailored from the TMF@SP4 film under one sun irradiation. The combination of MPCM and PDMS enables outstanding mechanical properties of the composite film material (Figures S19, S20, Supporting Information). The elongation at break of TMF@SP4-2 is 143.3%, surpassing that of the pure PDMS film (105.6%). We attribute the enhancement in mechanical properties primarily to the

**ADVANCED
SCIENCE NEWS**

www.advancedsciencenews.com

**ADVANCED
MATERIALS**

www.advmat.de
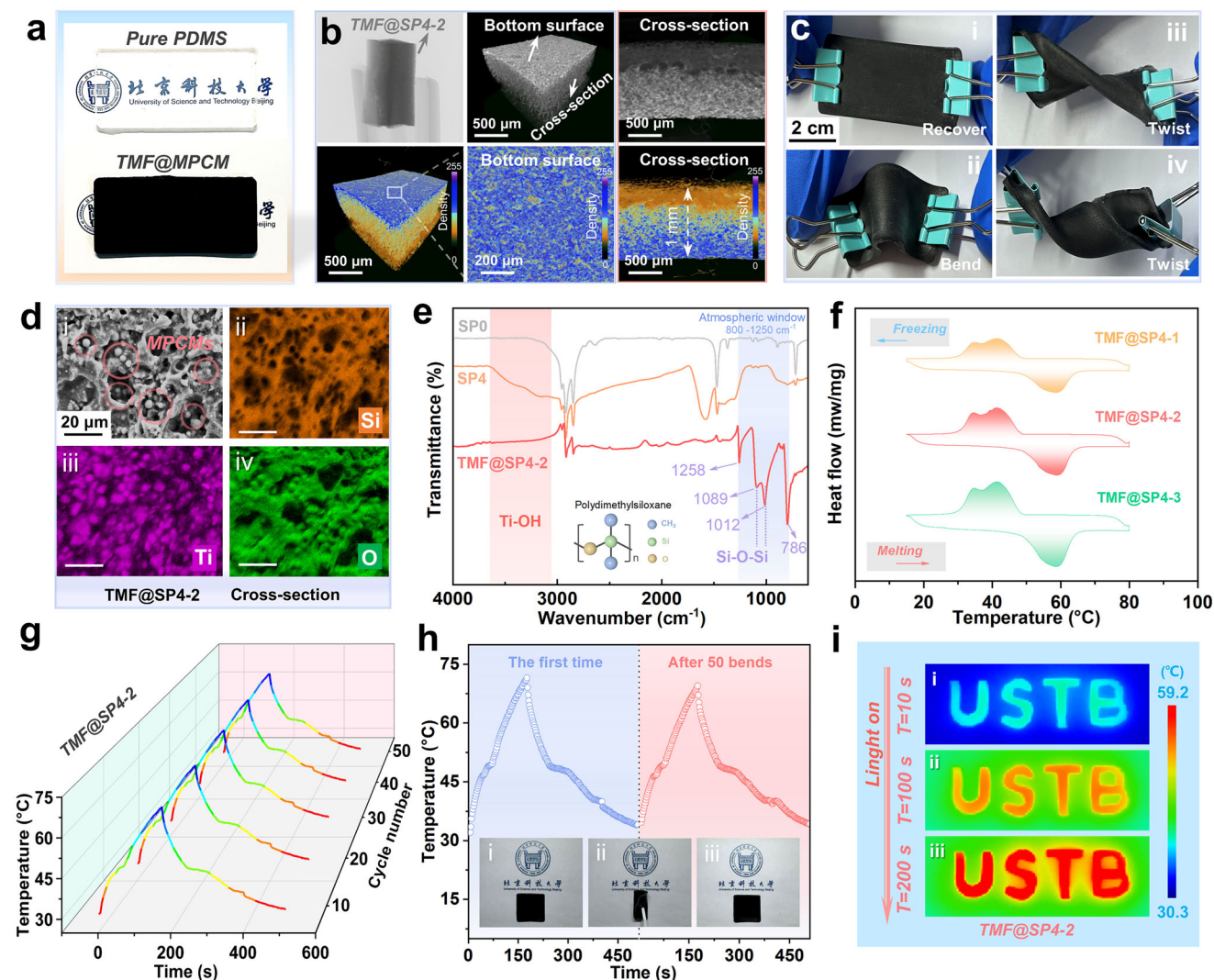
Figure 3. Comprehensive properties of the tri-mode photothermal, phase-change, and radiative-cooling films. a) Optical images of PDMS and TMF@SP4-2. b) 3D reconstructed tomography of TMF@SP4-2. c) Photographs of the TMF@SP4-2 film with different shapes. d) SEM and EDX images of TMF@SP4-2. e) FTIR spectra of SP0, SP4, and TMF@SP4-2. f) DSC heating and cooling thermograms of TMF@MPCM. g) Multicycle photothermal diagrams of TMF@SP4-2. h) Photothermal performance of TMF@SP4-2 before and after 50 bending tests. i) IR images of the cut USTB pattern with TMF@SP4-2 under one sun illumination.

formation of interface Si—O—Ti bonds between the PDMS matrix and TiO$_2$-based microcapsules, which can be confirmed by high-resolution O 1s XPS spectra (cf. Figure S13, Supporting Information). The chemical bonding at the interface optimizes the stress transfer pathway between the soft matrix and hard filler, significantly improving the mechanical properties of the film.[19] Such remarkable flexibility renders TMF@SP4-2 highly prospective for applications in fields such as wearable smart temperature control, high-voltage cables, and photothermal electricity.

2.4. Indoor Characterization of Solar-Thermal-Electric Conversion Performance

Based on the principle of the Seebeck effect, TEGs are capable of directly converting thermal energy into electrical energy, and the

voltage delivered by the TEGs depends on the temperature difference ($\Delta T = T_{hot} - T_{cold}$) between the hot and cold ends.[2c,4f,20] As shown in **Figures 4a** and S21 (Supporting Information), the TMF@SP4-2 composite film was adhered to the hot end of the TEG with thermal conductive silicon, while the heat dissipation aluminum fin was bonded to the cold end to constitute a TES. Under the irradiation of the xenon lamp, the composite film elevated the temperature of the hot end of the TES, while the aluminum fins maintained the cold end at room temperature, thereby generating a temperature difference on the TES and yielding output electrical energy. In order to provide a more stable V_o and further enhance the temperature difference, the heat sink was placed in water at a constant temperature of 26 °C. Figure 4b,c, and Figure S22 (Supporting Information) demonstrated the maximum V_o current and power density of the TES under various cold-end environments and different light intensities. Figure 4d–f illustrates
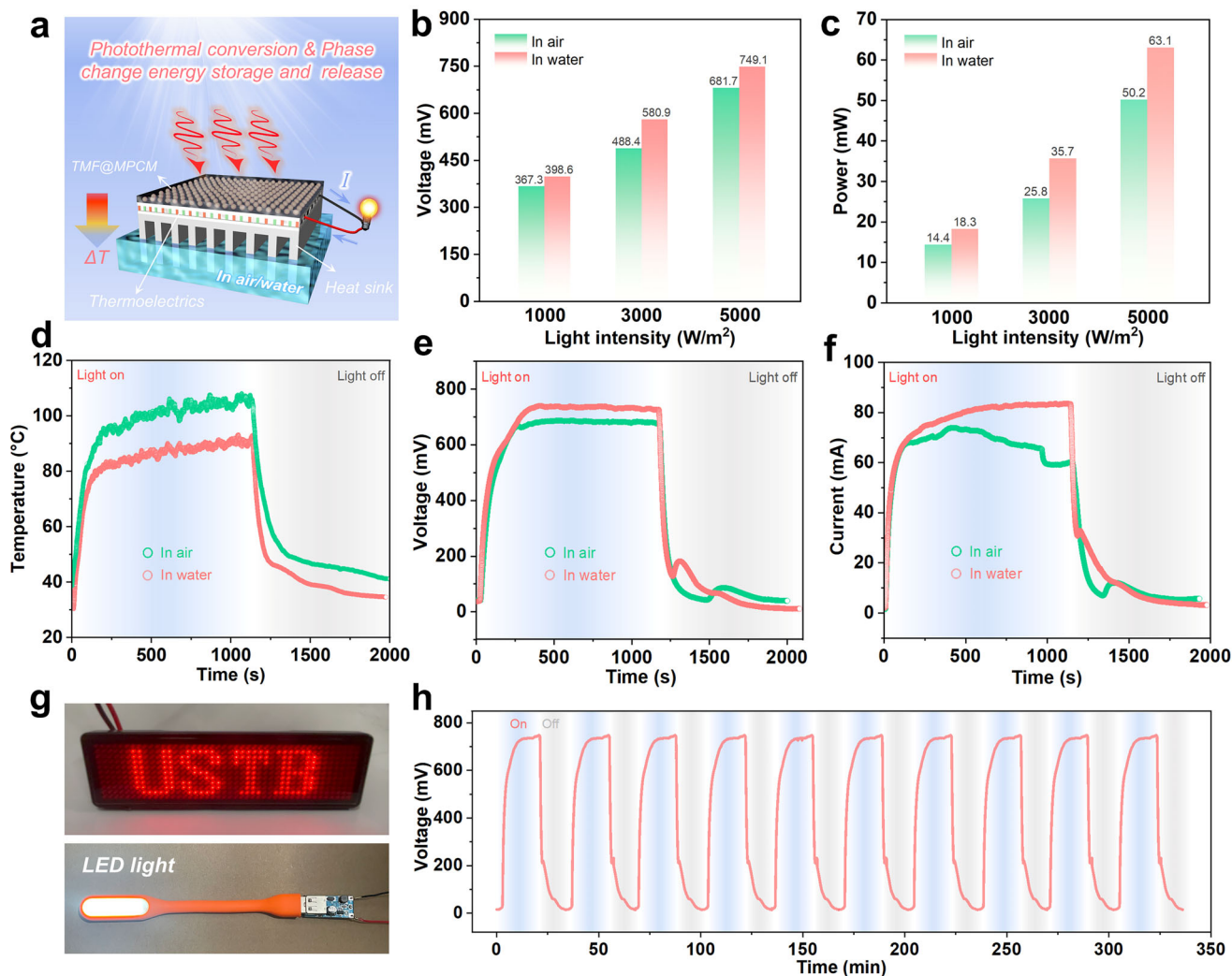
Figure 4. Photothermoelectric conversion properties of composite films. a) Schematic of the TES. b) Maximum output voltage and c) output power histograms of TES under light intensities of 1000, 3000, and 5000 W m^{-2}. d) Temperature (node 1)-time curves, e) Voltage-time, and f) Current-time curves of the TES under light intensities of 5000 W m^{-2}. g) Use the TES to power the lamp and the LED light. h) Ten voltage-time cycling curves of the TES under light intensity of 5000 W m^{-2}.

the temperature-time curve of the hot end (node 1), the voltage-time and current-time curves of the TES under a light intensity of 5000 W m^{-2}. Figure S23 (Supporting Information) shows the time-temperature curves of the cold end (node 2) in two distinct heat dissipation environments under the identical light intensity. In contrast to the circumstance where the cold end was placed in constant-temperature water, when the cold end was exposed to air, the temperature of the hot end of the TES was higher, but the maximum V_o was lower. This is attributed to the fact that under the air heat dissipation condition, the ΔT of the TES was smaller, and the temperature fluctuation was greater, giving rise to a more significant fluctuation in the output current (Figure 4f). When the cold end was placed in constant-temperature water, the maximum V_o, current, power, and power density of the TES attained 749.1 mV, 84.2 mA, 63.1 mW, and 21.1 W m^{-2}, respectively (Figure 4b,c; Figure S22, Supporting Information). Upon cessation of xenon lamp illumination, the V_o of the TES promptly declined due to the reduction in the hot end temperature. When the hot end temperature descended to the solidification temperature, the PCM initiated the release of the stored heat, thereby enabling the TES to continue providing voltage and current for a certain period. By releasing the thermal energy stored in the PCM to sustain the hot end temperature, the TES could still maintain discharge for over 800 s. We connected the TES as a power supply to the light-emitting diode (LED) spelling out "USTB" and a small light bulb (Figure 4g). The experimental results indicated that the electrical energy produced by the TES could successfully light up the LED. Furthermore, for the photothermal-electric cyclic performance of TMF@SP4-2, we conducted a continuous 335 min light-on/off test (Figure 4h) to evaluate its sustained photothermal-to-thermoelectric effect. Specifically, under light intensities of 1000 W m^{-2} (Figure S24, Supporting Information) and 3000 W m^{-2} (Figure S25, Supporting Information), the TES also exhibited stable electrical energy output. The TMF@SP4-2

**ADVANCED
SCIENCE NEWS**

www.advancedsciencenews.com

**ADVANCED
MATERIALS**

www.advmat.de
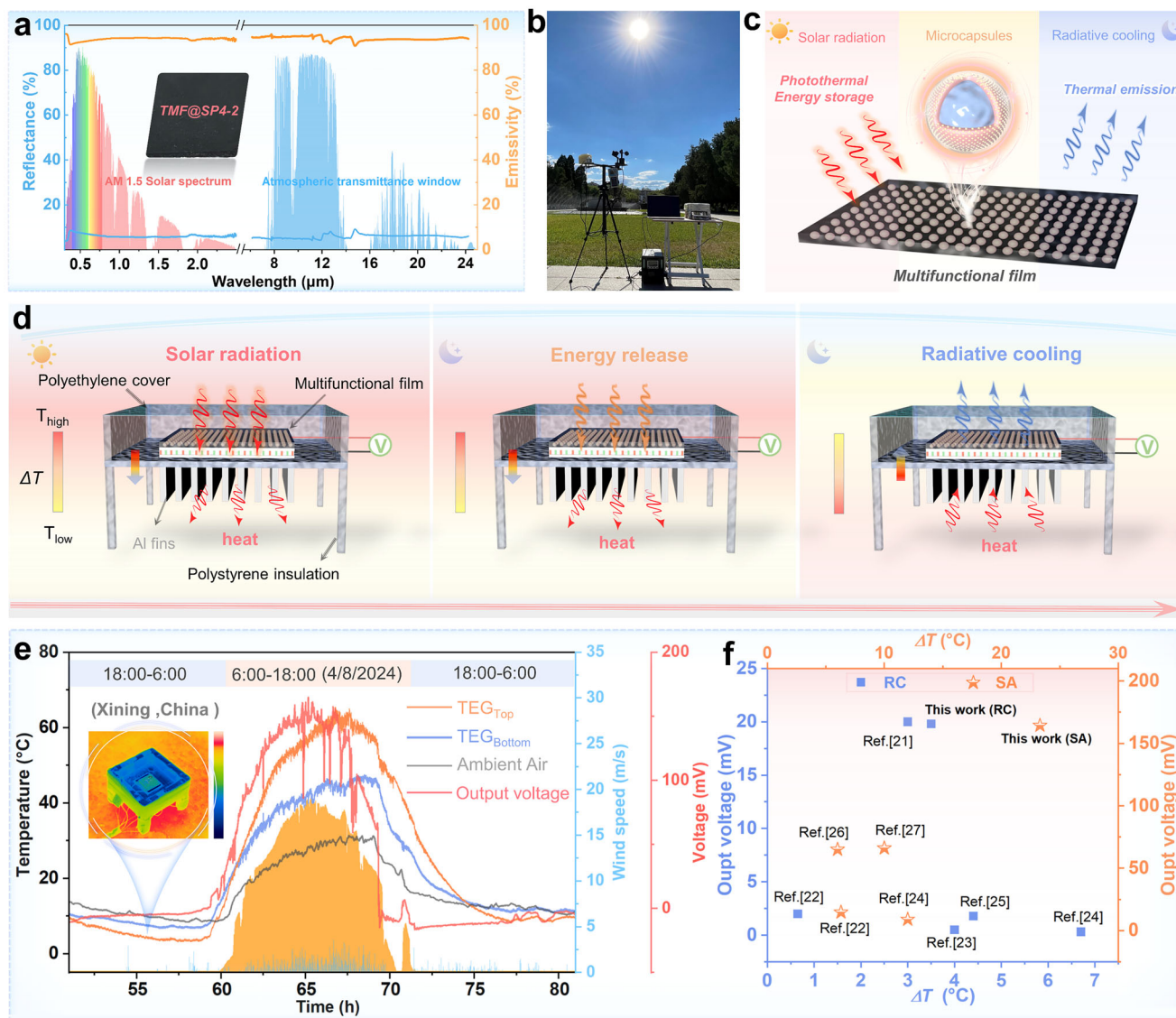
Figure 5. Radiative cooling and solar-thermal-electric conversion properties of TES. a) The TMF@SP4-2 films from the UV to the mid-infrared wavelength. The colorful shadow indicates the solar irradiance of AM 1.5, while the blue shadow indicates the atmospheric transmittance. b) The self-made photothermal-electric device. c) Diagram of the working mechanism of the multifunctional composite film. d) Schematic diagram of the working principle of the TES. e) Field measurements of TES in continuous uninterrupted operation in Xining, China. f) Performance comparison of the TES for energy collection from the sun (SA) and cold space (RC). Ishii et al.,[21] Xia et al.,[22] Mu et al.,[23] Chen et al.,[24] Xia et al.,[25] Zhang et al.,[26] Liao et al.[27] and this work.

endows the TES with an extremely competitive output power density and enables it to continuously and stably output power even in the absence of light conditions (Figure S26 and Table S4, Supporting Information).

2.5. Outdoor Performance of Radiative Cooling Coupled with Solar Thermal Power Generation

Although the TES has been demonstrated to offer efficient and stable power output, it's still unable to satisfy the demands of long-term consecutive application. Radiative cooling (RC), as an emerging passive cooling approach, is currently regarded as the most effective means of generating temperature differences at night. To assess the RC performance of the composite film under actual environmental circumstances, we conducted tests on the absorptivity and emissivity of the TMF@SP4-2 film throughout the entire spectral range. As shown in **Figure 5a**, the thin-film material attained an average absorptivity of 93.91% within the solar spectral range of 0.25 to 2.5 μm. Furthermore, in the first and second atmospheric windows (8–13 μm), the average emissivity of the film was 93.81% and 93.82%, respectively. This property can be elucidated by the FTIR spectrum of TMF@SP4-2 in Figure 3d. Specifically, the film exhibited three prominent absorption peaks within the wavenumber range of 800 to 1250 cm^{-1} (corresponding to 8–12.5 μm), which were closely associated with

ADVANCED
SCIENCE NEWS

www.advancedsciencenews.com

**ADVANCED
MATERIALS**

www.advmat.de

the vibration modes of Si—O—Si and Si—CH$_3$ bonds. Owing to the substantial coincidence of the energy range of these absorption peaks with the atmospheric windows, the film demonstrates high emissivity within this wavelength range.[16] The emissivity spectrum analysis of TMF@SP4-2 composite film demonstrated significant overlap with the atmospheric transparency window (8–13 µm) (Figure S27, Supporting Information). This overlap indicated that TMF@SP4-2 effectively utilized the atmospheric window for thermal radiation, achieving efficient passive radiative cooling.

In light of the remarkable light absorption capacity of the TMF@SP4-2 film within the solar spectrum and its high emissivity within the atmospheric window, our TES is expected to achieve 24 h uninterrupted electricity generation through PTC during the day and RC at night. To this end, we designed and self-fabricated a photothermal-electric device, in which the TES was placed inside a box filled with polystyrene foam and sealed with a high-transparency low-density polyethylene (LDPE) film on the top as a transparent window to minimize non-radiative convective and conductive heat exchange between the TES and the surrounding environment (Figure 5b; Figure S28, Supporting Information). The entire testing system was monitored in real-time in outdoor environments across multiple cities with distinct climatic characteristics (Table S5, Supporting Information). Figure 5c demonstrates the energy conversion mechanism of the composite film, while Figure 5d shows its all-day TES operational principle. The TES device generates electricity based on three temperature difference mechanisms: during the day when sunlight is abundant, the composite film operates in PTC mode using microcapsules to efficiently convert solar energy into thermal energy and achieves phase change heat storage; after the disappearance of light, the film's temperature drops to the solidification temperature of the PCM, releasing stored heat to maintain the temperature gradient within the TES until the heat is exhausted; at night, the film operates in RC mode, cooling the TES end facing the sky to lower temperatures than the other end, continuously generating a temperature difference and producing output power. The multi-mode functionality of the TES ensures uninterrupted power generation throughout the 24 h of the day.

Figure S29 (Supporting Information) and Figure 5e displayed the experimental validation results over four consecutive days in Xining City, Qinghai Province, China (36.3°N, 101.7°E) (the humidity data were shown in Figure S29, Supporting Information). During the midday period (11:00–14:00), the peak solar irradiance was ≈1200 W m^{-2}, the relative humidity was ≈30%, and the average ambient temperature was ≈29.3 °C. At this juncture, the temperature at the hot end of the TES during the day could reach a maximum of 68.2 °C, with a maximal temperature differential of 23.2 °C, corresponding to a V_o of 164.3 mV. At night, owing to the outstanding RC performance of the composite film, the TES device can continue to generate temperature differences through the RC mode. As shown at the bottom of Figure S29 and in Table S6 (Supporting Information), the average maximum nighttime temperature difference was ≈3.1 °C, with a corresponding average output voltage of 9.2 mV, and the highest recorded voltage was 18.9 mV. These results indicate that the TES can maintain thermoelectric output passively through RC even under zero solar radiation. The IR thermal imaging inset in Figure 5e highlighted the RC effect of the composite film at night, while Figure

S30 (Supporting Information) emphasized its PTC effect. To evaluate regional adaptability, we also conducted experiments in two cities with distinct climatic conditions in China, Xi'an and Beijing (Figures S31, S32 and Tables S5 and S6, Supporting Information). Specifically, in Xi'an, the maximum daytime temperature of the composite film could reach 75.4 °C, and the maximum temperature difference and V_o of the TES were 10.9 °C and 149.8 mV, respectively. At night, the maximum temperature difference was 2.5 °C, corresponding to a V_o of 12.1 mV. When the TES was placed in Beijing, the maximum daytime temperature of the composite film could reach 63.1 °C, with a maximum temperature differential of 12.3 °C and a corresponding V_o of 152.8 mV. At night-time, the maximum temperature difference was 3.2 °C, and the maximum V_o was 17.1 mV (see Table S6, Supporting Information). Overall, all the continuous outdoor experiments (Figures S29, S31, S32, Supporting Information) demonstrated that our TES device could adaptively harvest energy from both the sun and cold space, exhibiting superior stability and environmental adaptability compared to numerous reported TES (Figure 5f; Table S7, Supporting Information). Table S8 (Supporting Information) summarizes the main characteristic parameters of the SP4 microcapsules and TMF@SP4-2-integrated TES to provide a comprehensive understanding of this work. To provide a valuable reference for potential engineering applications of our TES, we evaluated the global distribution of the average annual output power density of the TES at a standard solar irradiance (6.1 W m^{-2}, 1 sun). As shown in Figure S33 (Supporting Information), simulated predictions were made using real-time meteorological data provided by Energyplus,[28] including ambient temperature, cloud cover, wind speed, etc. The output power density gradually decreased with the reduction of solar radiation intensity from the equator toward the poles. In certain coastal areas, highlands, and high-latitude regions, the output power is relatively low due to increased cloud cover and reduced sunlight exposure. Conversely, in several major desert regions such as the Sahara Desert, Australian Desert, and North American Desert, the output power is significantly higher due to low annual rainfall and prolonged periods of sunlight.

3. Conclusion

In summary, we designed and synthesized a type of microcapsule material for efficient photothermal conversion that featured full-spectrum absorption, high emissivity, and high latent heat storage density. Experimental results indicated that the microcapsules exhibited a latent heat of 144.5 J g^{-1} and a complete (100%) energy storage capacity, the thermal conductivity was 271.5% higher than that of pure organic PCM, and it demonstrated an outstanding PTCE of 93.7%. Additionally, after undergoing 200 cycles of DSC and 50 cycles of PTC, the phase change temperature and enthalpy of the microcapsules exhibited scarcely any variation, which was primarily attributed to their high encapsulation efficiency, ensuring no leakage of PCM during the cycling process. Furthermore, we exploited the abundant Ti—OH groups on the surface of the microcapsules to be composited with PDMS, fabricating a multifunctional film material. This film material can be integrated with thermoelectric modules to constitute an adaptive TES capable of continuously extracting energy from the sun and cold space for 24 h

ADVANCED
SCIENCE NEWS

www.advancedsciencenews.com

ADVANCED
MATERIALS

www.advmat.de

uninterruptedly. Under conditions where the light intensity ranges from 1000 to 5000 W m^{-2} and a constant-temperature water bath (initial temperature ≈26 °C) is used as the heat sink, the output power density of the TES device with TMF@SP4-2 film as the hot end ranged from 6.1 to 21.1 W m^{-2}. Even in the absence of illumination, the system can still generate electricity by releasing the latent heat from the PCM. Through actual outdoor tests, the system has successfully achieved 24 h continuous power generation in multiple cities. During the day, it can achieve a maximum temperature difference of 23.2 °C, and at night, 3.5 °C, corresponding to the maximum V_o of 164.3 and 18.9 mV, respectively. The materials design in this work offers a novel approach for the storage and reuse of solar energy and holds significant scientific importance for the development of all-day thermoelectric power generation technology.

4. Experimental Section

Materials and Reagents: Analytical grade tetra butyl titanate (TBT) and titanium (III) oxide were supplied from Aladdin Chemical Company Ltd., Shanghai, China. n-Tetracosane with a high purity of 99% and sodium dodecylbenzene sulfonate (SDBS) were purchased from Acros Organics Company, USA. Formamide was purchased from Anhui Zesheng Technology Co., Ltd., China (Energy Chemical). Petroleum ether and anhydrous ethanol were procured from Sinopharm Chemical Reagent Co., Ltd., China. Sylgard 184 silicone elastomer (consisting of a base and a curing agent at a weight ratio of 10:1), a common polydimethylsiloxane (PDMS) prepolymer kit, was purchased from Dow Corning, which was used as the matrix for preparing the composites. Hexyl hydride was purchased from Alfa Aesar, USA. All reagents were used as received without further purification.

Preparation of Microencapsulated Phase Change Materials: The preparation process and mechanism of solar-driven phase change microcapsules are shown in Figure 1a. In a typical synthesis, 3 g of n-Tetracosane is placed in a flask and stirred at 65 °C until completely melted. Then, 3 mL of TBT was added and mixed for 0.5 h. Subsequently, 60 mL of 0.03 M SDBS formamide solution was added and stirred continuously for 3 h to form a uniform and stable O/W emulsion. Next, 0.6 g of deionized water was mixed with 20 mL of formamide solution, and this mixture was added dropwise to the emulsion at the same stirring rate. Deionized water induced the hydrolysis of TBT, and the titanium dioxide precursor underwent interfacial condensation. Pre-milled Ti_2O_3 nanopowder dispersions of 0.01, 0.03, 0.05, and 0.07 g were then added dropwise, and the mixture was gently stirred at 65 °C for 4 h to form a solid TiO_2/Ti_2O_3 composite shell. The collected black powder was dried in a vacuum oven at 40 °C for 48 h to obtain a series of composite microcapsules with different Ti_2O_3 contents, designated SP2, SP3, SP4, and SP5, respectively. The microcapsules without Ti_2O_3 were designated SP1, and pure n-Tetracosane was designated SP0.

Preparation of Tri-Mode Film Materials: The preparation process of the tri-mode photothermal, phase-change, and radiative-cooling film is shown in Figure S10 (Supporting Information). A typical procedure first involved mixing a certain amount of PDMS with a curing agent (in a 10:1 ratio), followed by the addition of 30 mL of n-Hexane for dispersion. Subsequently, SP4 microcapsules of different mass fractions were added and uniformly stirred for complete mixing. The resulting mixture was transferred into a custom-made polytetrafluoroethylene mold and cured at 60 °C in a drying oven for 4 h, yielding PDMS-based composite films. When the mass fractions of SP4 were 40%, 60%, and 80%, the resulting series of composite films were labeled as TMF@SP4-1, TMF@SP4-2, and TMF@SP4-3, respectively. Additionally, a pure PDMS film without microcapsules was prepared as the control sample.

Solar-Thermal Energy Conversion Measurement of Microcapsules: The schematic of the photothermal test system is shown in Figure S8b (Supporting Information). A PLS-SXE300C xenon lamp equipped with a standard AM1.5 G optical filter was used as a simulated solar light source in a homemade thermal barrier, and the light intensity was calibrated by a PL-MW2000 optical power meter. The prepared MPCMs were individually pressed into thin slices (Diameter: 15 mm, Height: 2 mm) and exposed to a simulated xenon lamp with a light intensity of 1000 W m^{-2}. Time-temperature data were recorded in real time using a data collector (OMEGA), and the surface temperatures of the samples were measured by T-type thermocouples with a measurement accuracy of ±1 °C (0–350 °C) and a data acquisition interval of 0.05 s. An infrared image was captured using a FLIR A615 infrared camera to visualize the temperature change of the MPCM during the photothermal conversion process. The photothermal conversion efficiency of the samples could be calculated by dividing the latent heat of the MPCM by the photothermal energy according to Equation 5.

Solar-Thermal-Electric Energy Conversion Measurements: The TES consisted of a computer, a power supply, a T-type thermocouple, a data collector, a weather station, and a thermoelectric test module. The schematic diagram of the indoor experimental setup is shown in Figure S21 (Supporting Information), while the outdoor experimental setup is illustrated in Figure S28 (Supporting Information). The TES test module included a temperature difference generator plate and heat-dissipating aluminum fins. The temperature difference power generator and the TMF@SP4-2 film, each measuring ≈55 × 55 mm^2, were bonded to the heat source side of the power generator plate using QM850 thermally conductive silicone grease. The cold-source side of the plate was attached to the aluminum fins with the same silicone grease. The aluminum fins were placed in two different heat dissipation environments: ambient air, water at an initial temperature of ≈26 °C. The TES generator was then exposed to simulated xenon lamps with light intensities of 1000, 3000, and 5000 W m^{-2}, respectively. To characterize the temperature variations of the TMF@SP4-2 film during TES conversion and cooling, a T-type thermocouple was inserted at the bottom of the sample, and temperatures were recorded every 0.05 s using a data collector. The V_o and current of the TES were measured in real time with a multimeter. To visualize the output power, the TES was connected to an external circuit to power an LED with USTB patterns and light bulbs as analog loads. For the outdoor tests, the entire system was moved outside to evaluate the photothermoelectric effect and radiative cooling performance of the composite films in different geographical locations and climatic conditions, including Beijing, Xi'an, and Xining, China (see Table S5, Supporting Information). Additionally, a weather station was used to monitor local solar irradiance, wind speed, and relative humidity in real time.

Calculations of thermal storage capacity, photothermal conversion efficiency, and emissivity

$$E_{en} = \frac{\Delta H_{m,MPCM}}{\Delta H_{m,PCM}} \times 100\% \tag{1}$$

$$E_{es} = \frac{\Delta H_{m,MPCM} + \Delta H_{c,MPCM}}{\Delta H_{m,PCM} + \Delta H_{c,PCM}} \times 100\% \tag{2}$$

$$C_{es} = \frac{(\Delta H_{m,MPCM} + \Delta H_{c,MPCM}) \cdot \Delta H_{m,PCM}}{(\Delta H_{m,PCM} + \Delta H_{c,PCM}) \cdot \Delta H_{m,MPCM}} \times 100\% \tag{3}$$

where $\Delta H_{m,MPCM}$ and $\Delta H_{c,MPCM}$ denote the melting and crystallization enthalpies of MPCM, respectively; $\Delta H_{m,PCM}$ and $\Delta H_{c,PCM}$ are the melting and crystallization enthalpies of PCM, respectively.

$$\varepsilon = 1 - \rho - \tau \tag{4}$$

where m is the total mass of the sample, ΔH is the melting enthalpy is measured by DSC, P is the light intensity of the xenon lamp, and S is the illumination area of the sample. T_t and T_s are the onset and termination times of the phase change, respectively.

The emissivity (ε) of the composite films was then calculated by using the equation:

$$\eta = \frac{m \times \Delta H}{P \times S \times (T_t - T_s)} \times 100\% \tag{5}$$

where (ρ) and (τ) are the reflectance and transmittance, respectively.

Supporting Information

Supporting Information is available from the Wiley Online Library or from the author.

Conflict of Interest

The authors declare no conflict of interest.

Data Availability Statement

The data that support the findings of this study are available from the corresponding author upon reasonable request.

[1] a) A. P. Raman, W. Li, S. Fan, *Joule* **2019**, *3*, 2679; b) N. Xu, P. Zhu, Y. Sheng, L. Zhou, X. Li, H. Tan, S. Zhu, J. Zhu, *Joule* **2020**, *4*, 347.

[2] a) Y. Qin, B. Qin, D. Wang, C. Chang, L.-D. Zhao, *Energy Environ. Sci.* **2022**, *15*, 4527; b) T. Sun, L. Wang, W. Jiang, *Mater. Today* **2022**, *57*, 121; c) Q. Zhang, A. Huang, X. Ai, J. Liao, Q. Song, H. Reith, X. Cao, Y. Fang, G. Schierning, K. Nielsch, S. Bai, L. Chen, *Adv. Energy Mater.* **2021**, *11*, 2101213.

[3] a) M. Hong, J. Zou, Z. G. Chen, *Adv. Mater.* **2019**, *31*, 1807071; b) A. Witze, *Nature* **2014**, *515*, 484; c) B. T. McGrail, A. Sehirlioglu, E. Pentzer, *Angew. Chem. Int. Ed. Engl.* **2015**, *54*, 1710; d) S. Zhang, Z. Liu, Z. Wu, Z. Yao, W. Zhang, Y. Zhang, Z. Guan, H. Lin, H. Cheng, E. Mu, J. Zeng, C. Dun, X. Zhang, J. C. Ho, Z. Hu, *Nano Energy* **2024**, *132*, 110381.

[4] a) W.-W. Zhang, Y.-M. Guo, M.-J. He, Y.-T. Ren, B.-H. Gao, H. Qi, *Appl. Therm. Eng.* **2024**, *243*, 122063; b) S. Ishii, C. Bourgès, N. K. Tanjaya, T. Mori, *Mater. Today* **2024**, *75*, 20; c) C.-H. Wang, H. Chen, Z.-Y. Jiang, X.-X. Zhang, F.-Q. Wang, *Appl. Energy* **2023**, *331*, 120425; d) X. Li, Z. Zhang, X. Zhang, Y. Cao, Y. Yang, W. Wang, J. Wang, *Adv. Sci.* **2024**, *11*, 2308200; e) G. Wang, Z. Tang, Y. Gao, P. Liu, Y. Li, A. Li, X. Chen,

Chem. Rev. **2023**, *123*, 6953; f) S. Zhang, Z. Liu, X. Zhang, Z. Wu, Z. Hu, *The Innovation* **2024**, *5*, 1005981.

[5] a) M. Hou, Z. Jiang, W. Sun, Z. Chen, F. Chu, N. C. Lai, *Adv. Mater.* **2023**, *36*, 2313 12; b) M. Zare, K. S. Mikkonen, *Adv. Funct. Mater.* **2023**, *33*, 213455; c) M. Hou, Z. Jiang, F. Chu, X. Zhang, N.-C. Lai, *Colloids Surf., A* **2022**, *651*, 129674.

[6] J. Xiong, Z. Sun, J. Yu, H. Liu, X. Wang, *Chem. Eng. J.* **2022**, *430*, 132982.

[7] R. Liu, S. Wang, Z. Zhou, K. Zhang, G. Wang, C. Chen, Y. Long, *Adv. Mater.* **2024**, *29*, 1603730.

[8] a) J. Wang, Y. Li, L. Deng, N. Wei, Y. Weng, S. Dong, D. Qi, J. Qiu, X. Chen, T. Wu, *Adv. Mater.* **2017**, *29*, 1603730; b) X. Cui, Q. Ruan, X. Zhuo, X. Xia, J. Hu, R. Fu, Y. Li, J. Wang, H. Xu, *Chem. Rev.* **2023**, *123*, 6891; c) Y. Liu, J. Zhao, S. Zhang, D. Li, X. Zhang, Q. Zhao, B. Xing, *Environ. Sci.: Nano* **2022**, *9*, 2264.

[9] a) Y. Ren, M. Hou, Z. Jiang, W. Sun, F. Chu, N.-C. Lai, *Surf. Coat. Technol.* **2024**, *485*, 130888; b) Z. Chen, J. Zhang, S. Deng, M. Hou, X. Zhang, Z. Jiang, N.-C. Lai, *Chem. Eng. J.* **2023**, *454*, 140089; c) G. Zhou, M. Hou, Y. Ren, Z. Jiang, N.-C. Lai, *J. Energy Storage* **2023**, *72*, 108458; d) M. Hou, Z. Jiang, X. Zhang, W. Sun, F. Chu, N.-C. Lai, *Mater. Today Chem.* **2024**, *40*, 102205.

[10] H. Liu, D. Tian, Z. Zheng, X. Wang, Z. Qian, *Chem. Eng. J.* **2023**, *458*, 141395.

[11] M. Hou, H. Zheng, C. Wang, X. Zhang, Z. Jiang, N.-C. Lai, *Colloids Surf., A* **2025**, *710*, 136213.

[12] H. Chen, J. Liang, L. Li, B. Zheng, Z. Feng, Z. Xu, Y. Luo, Q. Liu, X. Shi, Y. Liu, S. Gao, A. M. Asiri, Y. Wang, Q. Kong, X. Sun, *ACS Appl. Mater. Interfaces* **2021**, *13*, 41715.

[13] Z. Cheng, Y. Hu, K. Wu, Y. Xing, P. Pan, L. Jiang, J. Mao, C. Ni, Z. Wang, M. Zhang, Y. Zhang, X. Gu, X. Zhang, *Electrochim. Acta* **2020**, *337*, 135789.

[14] K. Zhao, Z. Guo, J. Wang, H. Xie, *Chem. Eng. J.* **2023**, *471*, 144723.

[15] M. Liu, X. Li, L. Li, S. Zhao, J. Zhu, T. Zhou, Z. Lin, J. Li, B. Sun, G. Pei, B. Zhao, C. Zou, *Small* **2024**, *20*, 2403020.

[16] K. Lin, L. Chao, T. C. Ho, C. Lin, S. Chen, Y. Du, B. Huang, C. Y. Tso, *Energy Build.* **2021**, *252*, 111400.

[17] S. Li, Z. Lin, Z. Zhou, Y. Zhao, Z. Ling, Z. Zhang, X. Fang, *Nanoscale* **2023**, *15*, 3419.

[18] a) Z. Liu, Z. Liu, S. Ji, G. Wang, *Sci. Rep.* **2020**, *10*, 16750; b) X. Hui, R. Zhao, P. Zhang, C. Li, C. Wang, L. Yin, *Adv. Energy Mater.* **2019**, *9*, 1901065.

[19] a) X. Cai, X. Wang, F. Bian, J. Li, R. Zhou, J. Hu, S. Lin, *Chem. Eng. J.* **2024**, *498*, 154934; b) L. Wang, Y. Chen, L. Lin, H. Wang, X. Huang, H. Xue, J. Gao, *Chem. Eng. J.* **2019**, *362*, 89.

[20] a) X. L. Shi, L. Wang, W. Lyu, T. Cao, W. Chen, B. Hu, Z. G. Chen, *Chem. Soc. Rev.* **2024**, *53*, 9254; b) W. Li, B. Poudel, A. Nozariasbmarz, R. Sriramdas, H. Zhu, H. B. Kang, S. Priya, *Adv. Energy Mater.* **2020**, *10*, 2001924.

[21] S. Ishii, T. D. Dao, T. Nagao, *Appl. Phys. Lett.* **2020**, *117*, 013901.

[22] Z. Xia, Z. Zhang, Z. Meng, Z. Yu, *J. Quant. Spectrosc. Radiat. Transfer* **2020**, *251*, 107038.

[23] E. Mu, Z. Wu, Z. Wu, X. Chen, Y. Liu, X. Fu, Z. Hu, *Nano Energy* **2019**, *55*, 494.

[24] C. Chen, B. Zhao, R. Wang, Z. He, J. L. Wang, M. Hu, X. L. Li, G. Pei, J. W. Liu, S. H. Yu, *Adv. Mater.* **2022**, *34*, 2206364.

[25] Z. Xia, Z. Zhang, Z. Meng, L. Ding, Z. Yu, *ACS Appl. Mater. Interfaces* **2019**, *11*, 33941.

[26] S. Zhang, Z. Wu, Z. Liu, E. Mu, Y. Liu, Y. Lv, T. Thundat, Z. Hu, *Adv. Mater. Technol.* **2022**, *7*, 2200478.

[27] M. Liao, D. Banerjee, T. Hallberg, C. Åkerlind, M. M. Alam, Q. Zhang, H. Kariis, D. Zhao, M. P. Jonsson, *Adv. Sci.* **2023**, *10*, 2206510.

[28] https://energyplus.net/weather (accessed: April 2025).